Proteomic Profiling of a Layered Tissue Reveals Unique Glycolytic Specializations of Photoreceptor Cells*⍉

Boris Reidel‡, J. Will Thompson§, Sina Farsiu‡, M. Arthur Moseley§, Nikolai P. Skiba‡¶, and Vadim Y. Arshavsky‡¶

The retina is a highly ordered tissue whose outermost layers are formed by subcellular compartments of photoreceptors generating light-evoked electrical responses. We studied protein distributions among individual photoreceptor compartments by separating the entire photoreceptor layer of a flat-mounted frozen retina into a series of thin tangential cryosections and analyzing protein compositions of each section by label-free quantitative mass spectrometry. Based on 5038 confidently identified peptides assigned to 896 protein database entries, we generated a quantitative proteomic database (a "map") correlating the distribution profiles of identified proteins with the profiles of marker proteins representing individual compartments of photoreceptors and adjacent cells. We evaluated the applicability of several common peptide-to-protein quantification algorithms in the context of our database and found that the highest reliability was obtained by summing the intensities of all peptides representing a given protein, using at least the 5–6 most intense peptides when applicable. We used this proteome map to investigate the distribution of glycolytic enzymes, critical in fulfilling the extremely high metabolic demands of photoreceptor cells, and obtained two major findings. First, unlike the majority of neurons rich in hexokinase I, but similar to other highly metabolically active cells, photoreceptors express hexokinase II. Hexokinase II has a very high catalytic activity when associated with mitochondria, and indeed we found it colocalized with mitochondria in photoreceptors. Second, photoreceptors contain very little triosephosphate isomerase, an enzyme converting dihydroxyacetone phosphate into glyceraldehyde-3-phosphate. This may serve as a functional adaptation because dihydroxyacetone phosphate is a major precursor in phospholipid biosynthesis, a process particularly active in photoreceptors because of the constant renewal of their light-sensitive membrane disc stacks. Overall, our approach for proteomic profiling of very small tissue amounts at a resolution of a few microns, combining cryosectioning and liquid chromatography-tandem MS, can be applied for quantitative investigation of proteomes where spatial resolution is paramount. *Molecular & Cellular Proteomics 10: 10.1074/mcp.M110.002469, 1–14, 2011.*

The vertebrate retina is a layered tissue containing several types of neurons and supporting cells (1). The outermost half of the retina is formed by rod and cone photoreceptors, which produce electrical responses upon capturing photons. Photoreceptors are polarized neurons in which specific functions are carried out in individual highly specialized subcellular compartments. For example, the processes of light capturing and visual signaling are confined to the distal outer segment, whereas information transfer to the secondary retina neurons takes place at the synaptic terminal located at the opposite side of the cell. In this study, we analyzed the patterns of subcellular protein distribution in photoreceptors by label-free quantitative mass spectrometry.

Proteomic analysis of layered or intricately structured tissues requires a difficult analytical combination of reproducible sample preparation with high spatial resolution, significant depth of proteome coverage, and accurate quantification. These challenges have been addressed to varying degrees by laser-capture microdissection along with MS analysis and matrix assisted laser desorption ionization (MALDI)[1] imaging. Laser capture microdissection is typically performed following immunostaining for specific markers to define the regions of interest (2–7); although this approach has very high resolution (microns), the amount of material available for MS analysis is exceedingly small because of the limited thickness of tissue sections. MALDI imaging has the advantage of high speed and ease of sample preparation, but suffers from lower spatial resolution (typically hundreds of microns), inherent difficulty in protein identification, and limited depth of proteome coverage (8–13).

[1] The abbreviations used are: MALDI, matrix-assisted laser desorption ionization; ICC, intraclass correlation coefficient; DDA, data-dependent analysis; LC-MS/MS, liquid chromatography-tandem MS; CRALBP, cellular retinal aldehyde binding protein; PVDF, polyvinylidene fluoride; PLGS, protein lynx global server.

Unbiased quantitative label-free proteomics, utilizing liquid chromatography-tandem MS (LC-MS/MS), is a rapidly emerging methodology allowing comparison of protein contents across multiple samples, when utilizing the accurate-mass and time-tag approach for alignment of peptides across the samples (14–20). This technique requires accurate-mass, high-resolution mass spectrometers for data collection and sophisticated software for data analysis. Many open-source and commercial options are now available to perform the latter task (21–24). The label-free approach also has the advantage of unlimited scalability with respect to number of samples or number of experimental variables, provided that methods for sample preparation are sufficiently quantitative and control for analysis-to-analysis variability is carefully considered.

Taking advantage of the highly ordered retina structure, we obtained thin serial tangential sections through the rat outer retina, which contained proteins derived from different parts of the photoreceptor cells. Because the rat retina is dominated by rod photoreceptors (outnumbering cones by >100-fold (25)), the vast majority of photoreceptor-derived proteins in these sections originated from rods. In the past, we combined this technique with Western blot detection of individual proteins in sections, which provided an alternative to immunohistochemistry to study longitudinal protein distributions in these cells (26). This method resolved several long-standing controversies regarding the subcellular localization of photoreceptor-specific proteins, which arose from conflicting results of immunohistochemical studies (26–28). We now extended this methodology to analyze distribution profiles of hundreds of proteins by combining serial sectioning of the retina with quantitative mass spectrometry. The results are summarized in a database (which we call a proteome "map"), correlating the relative abundances of all identified proteins in individual serial sections with those of marker proteins representing specific compartments of photoreceptors and neighboring cells. We used this map to assess the subcellular distribution of all glycolytic enzymes and uncovered novel patterns for the two hexokinase isoforms and triosephosphate isomerase, each likely reflecting the unusually high metabolic activity of photoreceptor cells.

EXPERIMENTAL PROCEDURES

Animals—Sixty-day-old pigmented Long-Evans rats (*Rattus norvegicus*) were purchased from Charles River Laboratories (Wilmington, MA). Animals were dark-adapted for at least 12 h and sacrificed under dim red light either immediately or following one hour exposure to bright light producing 15,000 lux on the cornea surface as described in (29).

Serial Tangential Sectioning of the Rat Retina—Serial sectioning was performed as described in (26) with modifications described in (29) and (30). Briefly, eyes were enucleated from an anesthetized rat and dissected in ice-cold Ringer's solution under dim red light. A retina fragment (3 mm in diameter) was cut from the eyecup with a surgical trephine positioned right next to the optic disc (so that the optic nerve remained just outside the analyzed specimen), transferred onto PVDF membrane with the photoreceptor layer facing up, flat-mounted between two glass slides separated by plastic spacers (ca. 240 μm) and frozen on dry ice. Progressive tangential sections were then collected using a cryo-microtome following aligning the retina surface with the cutting plane of the microtome knife. The uneven edges of the retina specimen were trimmed and twelve 10-μm sections were collected.

Sample Preparation for Mass Spectrometry—A complete analysis was performed with two sets of retina sections, one obtained from a dark-adapted and another from a light-adapted rat referred as retinas #1 and #2, respectively, throughout the text. Each retina section was dissolved in 50 μl 0.5% v/v anionic acid liable surfactant II (Protea Biosciences, Morgantown, WV), followed by sonication and boiling for 5 min. Cysteine residues were reduced with 10 mM dithiothreitol and alkylated with 20 mM iodoacetamide. Proteins were digested with trypsin (15 ng/μl) overnight at 37 °C and anionic acid liable surfactant II was inactivated by adding trifluoroacetic acid to the final concentration of 1%. Samples were vacuum-dried and dissolved in 25 μl 0.1% trifluoroacetic acid and 2% acetonitrile. The typical amount of total protein in a section prepared as above was ~1.5 μg as determined by BCA assay in retina sections prepared identically to those analyzed by MS; no protein measurements were performed directly in samples used for MS in order to maximize the amount of material for analysis. We chose this gel-free protein digestion protocol in order to minimize any variability in peptide extraction and thus to improve quantitative aspects of the subsequent analysis.

LC/MS Data Collection—Peptide digests obtained from each of the 24 sections (12 from each retina) where analyzed using a nanoAcquity UPLC system coupled to a Synapt HDMS mass spectrometer (Waters Corp, Milford, MA). Approximately 500 ng of peptide material in 8 μl was first trapped at 20 μl/min for 2 min in 99.9% water with 0.1% v/v formic acid on a 20 μm × 180 mm Symmetry C18 column. Separations were then performed on a 75 μm × 250 mm column with 1.7 μm C18 BEH particles (Waters) using a 120-min gradient of 5 to 40% acetonitrile with 0.1% formic acid at a flow rate of 0.3 μl/min and 45 °C column temperature. We conducted two data-independent (MS^E) analyses of each retina section for simultaneous peptide quantification and identification. MS^E runs of samples obtained from different sections were performed in random order, and used 0.9 s cycle time alternating between low collision energy (6 V) and high collision energy ramp (15 to 40 V). The quantitative analyses were followed by an additional, supplementary LC-MS/MS experiment in the data-dependent analysis (DDA) mode for each section, using a 0.9 s MS scan followed by MS/MS acquisition on the top three ions with charge greater than one. MS/MS scans for each ion used an isolation window of ~3 Da, a maximum of 4 s per precursor, and dynamic exclusion for 120 s within 1.2 Da.

LC-MS Data Processing—For robust peak detection and label-free alignment of individual peptides across all 72 sample injections, we utilized the Rosetta Elucidator® v3.3 software (Rosetta Biosoftware, Inc., Seattle, WA) with PeakTeller algorithm, in a similar manner to several recent publications (24, 31–37). Following alignment and annotation, chromatographic peak intensities belonging to the same precursor mass in the MS^E aligned chromatograms were used to calculate the relative peptide and protein abundance on a section-by-section basis. Two MS^E analytical replicate intensities for each peptide were combined by averaging following robust median scaling (top and bottom 10% excluded), to generate one intensity value per peptide for each of the 24 photoreceptor layer sections.

We utilized both MS/MS DDA and MS^E to generate peptide identifications. For DDA acquisition files, .mgf searchable files were produced in Rosetta Elucidator and searches were then submitted to and retrieved from the Mascot v2.2 (Matrix Sciences, Inc) search engine in an automated fashion. For MS^E data, ProteinLynx Global Server 2.4 (Waters Corporation) was used to generate searchable files that were

then submitted to the IdentityE search engine (Waters Corporation, Milford, MA) (38, 39); results files were then imported back into Elucidator. To enable global spectra scoring across results from both search engines, all search results were concurrently validated using the PeptideProphet and ProteinProphet algorithms in Elucidator using independent reverse decoy database validation (40, 41). Peptides with PeptideProphet scores greater than 0.8 were then annotated; this score corresponded to a 2% peptide false discovery rate. Individual peptide scores are reported in supplemental Table 1. Each peptide identified was allowed to be assigned to a single protein entry, and these assignments were made by ProteinProphet according to the rules of parsimony, and ProteinProphet scores are provided in supplemental Table 1.

Both DDA and MS^E data were searched against the NCBInr database with *Rattus norvegicus* taxonomy (downloaded March 4, 2009 from http://www.ncbi.nlm.nih.gov/pubmed/), with full $1\times$ reverse database appended for peptide false discovery rate determination, and duplicates removed using Protein Digest Simulator Basic (http://omics.pnl.gov/software/ProteinDigestionSimulatorBasic.php). The final database contained 134914 sequences including reverse entries. Precursor ion mass tolerance was 20 ppm for both PLGS and Mascot searches, and product ion tolerance was 0.1 Da for Mascot and 40 ppm for PLGS. Enzyme specificity was set to semitryptic for Mascot searches and tryptic for PLGS 2.4 searches, and a maximum of two missed cleavages was allowed. Carbamidomethyl cysteine was included as a fixed modification, and variable modifications included oxidized methionine and deamidated asparagine and glutamine. Additionally, phosphorylation of serine, threonine, and tyrosine was allowed in Mascot searches (only nine phosphorylated peptides were observed).

LC-MS Data Quality Control—One quantitative data file from section #11 of the light-adapted retina, upon visual inspection, appeared to have inconsistent signal where significant portions of the data were missing, and therefore this file was removed from downstream analysis. Data quality control for the remaining 71 analyses was performed within the Elucidator software package by using the retention time viewer to assess the shift required for data alignment, and principal components analysis to assess consistency of data quality. The retention time shift required to properly align data files was evaluated for every LC-MS analysis. The maximum retention time shift required at any point across all 72 analyses was 2.1 min, with 62 analyses displaying shifts not exceeding 1 min. Peptide intensities for each sample were z-score transformed and submitted to a three-dimensional principal components analysis to look for analytical outliers. This analysis showed that the technical replicate injections were always separated by the smallest difference and in many cases the coordinated sections from each retina were also closely grouped (supplemental Fig. 1). No additional outliers were observed.

Intraclass Correlation Analysis of Protein Distributions Among Individual Retina Sections—To assess the reliability of several peptide-to-protein quantification algorithms we employed the intraclass correlation analysis, which is a statistical method used to describe correlation among results of similar experiments obtained by different experimental approaches or different observers (42). The degree of similarity among the results of individual experiments is reflected by the intraclass correlation coefficient (ICC). The ICC values and their 95% confidence intervals were calculated with the PASW Statistics software, version 18 (SPSS Inc., Chicago, IL), using the ICC(2,1) two-way random single measures (Consistency/Absolute agreement) option.

Data Alignment Among Protein Distribution Profiles Obtained from Individual Retinas—The retinal sectioning is not exactly the same from sample to sample reflecting imperfections in specimen preparation: freezing the retina may result in layer distortions causing three-dimensional waving and small variations in tissue compression (26). In addition, the thickness of the first section cannot be precisely controlled on the microtome. Therefore, averaging protein quantification data obtained from two retinas required an alignment of protein distribution profiles in sections obtained from each of them, so at least two of these variations (tissue compression and the first section thickness) could be accounted for. This was accomplished using phosducin as a representative protein, because it is an abundant protein distributed through the entire photoreceptor length and absent from the neighboring cell types (27, 43). The distribution profiles of phosducin were therefore modeled as piecewise cubic polynomials. To reduce boundary artifacts, the original 12 elements of the phosducin profile measurement vector obtained from each retina were padded by adding four extra elements in the beginning and at the end, creating a 20 element discrete representation of this profile (44). We set the values for the first and the last four elements of this vector equal to the fifth and 16th elements, respectively. We used "*cftool*" function of the MATLAB software (Mathworks, Natick, MA) to fit a piecewise cubic spline curve to each 20 elements profile. Next, we searched for the scaled affine transform that warps the phosducin profile in retina #1 to that in retina #2: $Y_1(x) = \frac{1}{c}Y_2(ax + b)$, where Y is the value of this profile at a distance x from the origin. We estimated the values of coefficients a, b and c by minimizing the following constrained least-squares cost function:

$$\hat{a},\hat{b},\hat{c} = \underset{a,b,c}{\mathrm{ArgMin}}\left(\left\|Y_1(x) - \frac{1}{c}Y_2(ax + b)\right\|_2^2\right)$$

$$\text{such that} \quad b \in [-1,1] \quad \text{and} \quad x \in [6,15],$$

where $\|...\|_2^2$ is the Euclidean norm. The constrain over b is evoked because the mismatch between the two section sets cannot be larger than a single section. The constrain over horizontal (x) search space is evoked because the first and last real sample points (elements 5 and 16 in our padded measurement vectors) and their replicas (elements 1 to 4 and 17 to 20) are most prone to the measurement noise. The calculated coefficients were: $\hat{a} = 0.8$, $\hat{b} = 0.95$, $\hat{c} = 1.1$. This procedure allowed us to define the data acquired in 10 μm imperfect

---

DDA data:	
oKkwTkOTW52kBbI8QOQOyL1CWR3576yJ81vNKSXDUaYRnsFFNRK8 sL8mz8cNxabVckCTuMM/OhvpWsLTtxAB94v39X4AAAAAAAACgg==	DDA data acquired from retina #1 and 2
MSE Data 1:	
5+MpeIU0BI/g/jn6JREUo7Tk73pKnGGizrT51BWESA8tde55IjI2g3y6wh3KGlSK o6lNSV1H8hbwwYmQfvTEqgSYMfUAAAAAAAADSA==	MS^E data acquired from retina #1
MSE Data 2:	
etkfeflM76zo5s7/K7cT7ll2XGClV6q8kqsIxOndeESgwVPIeEMRDQbq GnJQoiPQfsJzg54mMU/eXe/MWroh3sAo81kAAAAAAAAC3Q==	MS^E data acquired from retina #2

FIG. 1. **Schematic illustration of the serial sectioning technique, sample preparation, and MS workflow.** Twelve 10 μm-thick tangential sections were collected from the photoreceptor layer of a frozen flat-mounted rat retina (*left*; reproduced with permission from (26)). Each section was transferred into a 0.6-ml reaction tube (*middle panel*) and processed as described in the workflow on the right. Abbreviations: OS, outer segments; IS, inner segments; N, nuclear layer; ST, synaptic termini.
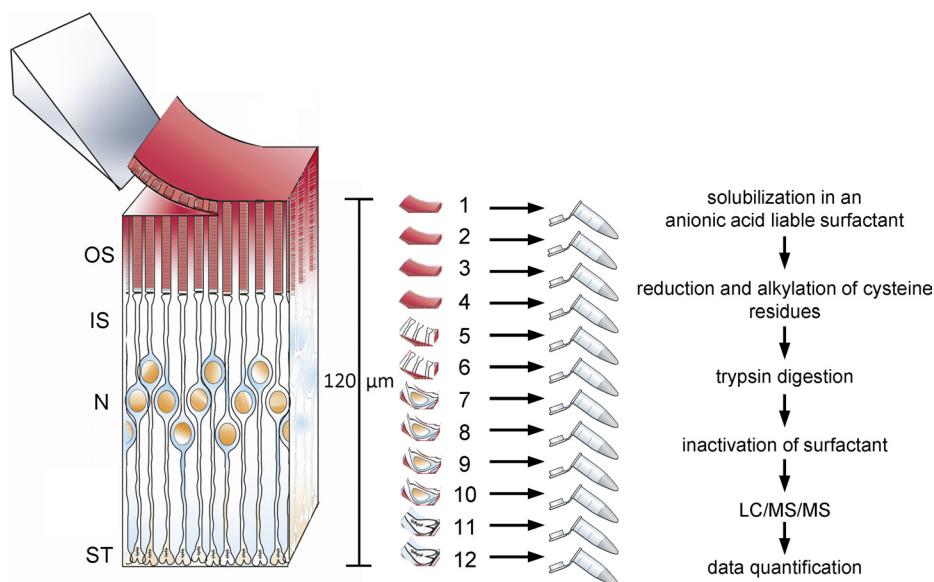
physical sections as a corrected distance from the distal end of the photoreceptor cell.

Immunohistochemistry—Immunofluorescence detection of selected proteins in the rat retina was performed as described previously (45); all experiments were performed in triplicate. Briefly, eye cups were fixed in paraformaldehyde and embedded in 4.5% low-melt agarose (Invitrogen). One hundred and fifty-μm-thick cross-sections of the retina were collected with a vibratome (Leica VT1200 S), incubated with blocking solution (3% goat serum and 0.1% Triton X-100 in phosphate-buffered saline), treated with primary antibodies overnight, washed and incubated with goat anti-rabbit Alexa Fluor 488 secondary antibodies (1:400). Stained sections were mounted with Fluoromount G (Electron Microscopy Sciences) under glass coverslips and visualized using a Nikon Eclipse 90i confocal microscope. Polyclonal rabbit antibodies against hexokinase I and against hexokinase II (1:200) were provided by J.E. Wilson (Department of Biochemistry, Michigan State University, East Lansing, MI), and antibodies against triosephosphate isomerase (FI-249) and GAPDH (sc-47724) were purchased from Santa Cruz Biotechnology(Santa Cruz, CA) (1:100). No signals were observed in control sections incubated with the secondary antibody only.

RESULTS AND DISCUSSION

Label-Free Protein Quantification in Retinal Serial Sections—To analyze the patterns of protein distribution along the longitudinal axis of the photoreceptor cell, we separated the entire photoreceptor layer from a frozen flat-mounted rat retina into 12 serial 10-μm-thick tangential sections and determined the relative abundance of individual proteins in each section by LC/MS (our workflow is illustrated in Fig. 1). The analysis of 24 sections obtained from two individual retinas yielded a total of 5038 unique peptides corresponding to 896 protein database entries (supplemental Table 1). This table contains intensity values for all peptides from each section, which were used for protein quantification. There are several approaches to translate information contained in peptide intensities determined in multiple biological samples into relative protein abundance in each sample. Many studies rely on

averaging the peptide intensity ratios of multiple peptides representing each protein in different samples (*e.g.* (36, 46–48)). Others average signals from the three most intense peptides (49) or sum signals from all peptides identified for a given protein (50–52). We, therefore, evaluated the accuracies of these protein quantification algorithms in application to our case.

Despite the unique protein composition of each section, there are several protein groups expected to preserve a constant molar ratio in all sections where they are found. These are proteins confined to specific cellular organelles, which maintain constant composition of their constituents regardless of their abundance in different sections. We applied four different quantification algorithms to generate the distribution profiles of proteins representing two organelles, the rod outer segment and the mitochondrion: (1) we expressed the peak area for the single most intense peptide from each protein as percentage distribution among all twelve sections; (2) we summed the peak areas for the three most intense peptides representing a given protein; (3) we summed the peak areas for all peptides from a given protein; (4) we calculated the fraction of each peptide present in each section and averaged the resulting values among all peptides representing a protein of interest. Note that in algorithms #2 and #3 peptides producing more intense peaks contributed to the resulting value with higher weights, whereas in algorithm #4 each peptide made an equal contribution to the resulting value. The reliability of protein quantification obtained using each algorithm was assessed by cross-correlating the resulting profiles of proteins representing each organelle. We used the intraclass correlation analysis (42), an ANOVA-based statistical methodology in which the degree of similarity among the individual protein profiles was reflected by the ICC, ranging from 0 to 1.
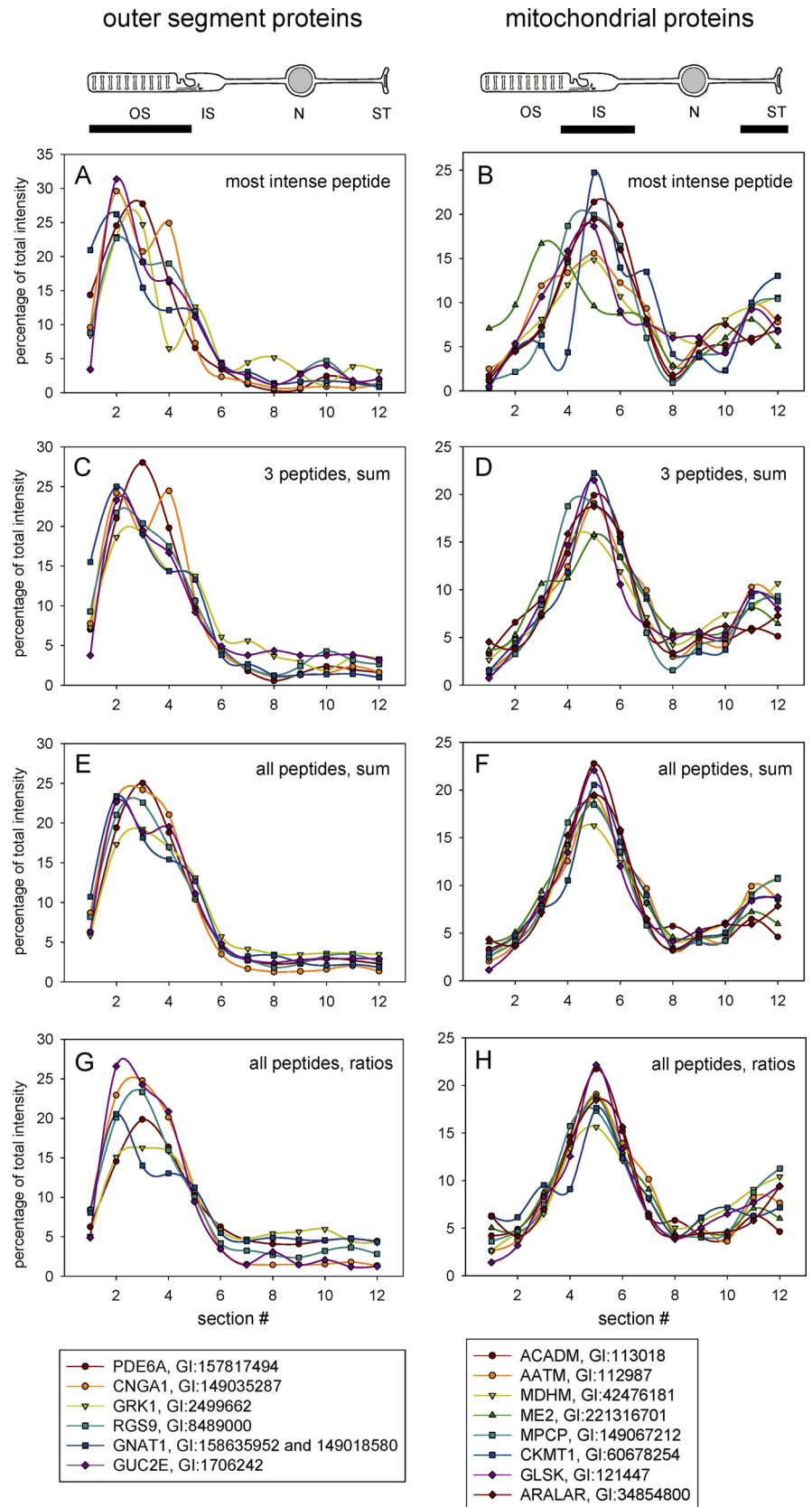
FIG. 2. **Distribution profiles of rod outer segment and mitochondrial proteins calculated by four peptide-to-protein quantification algorithms.** Data obtained for outer segment-specific proteins are shown on the *left* (*A–G*) and for mitochondrial proteins on the *right* (*B–H*). The plots are color-coded according to descriptions in the legends below the panels. Quantification algorithms used in each case are indicated in the panels. The subcellular localization of each protein group is indicated by black bars below the photoreceptor cell cartoons on the top. Abbreviations: OS, outer segment; IS, inner segment; N, nucleus; ST, synaptic terminal.

TABLE I
Intraclass correlation analysis of protein distribution profiles obtained by four different peptide-to-protein quantification algorithms

Peptide-to-protein algorithm	ICC[a] retina #1	95% CI[a] retina #1	ICC retina #2[b]	95% CI retina #2
Outer segment proteins				
Most intense peptide	0.88	0.76–0.96	0.93	0.84–0.98
Sum of 3 most intense peptides	0.92	0.89–0.98	0.95	0.89–0.98
Sum of all peptides	0.96	0.93–0.99	0.97	0.93–0.99
Ratios of all peptides	0.89	0.76–0.98	0.92	0.83–0.97
Mitochondrial proteins				
Most intense peptide	0.72	0.53–0.89	0.75	0.57–0.90
Sum of 3 most intense peptides	0.90	0.80–0.96	0.87	0.75–0.95
Sum of all peptides	0.93	0.87–0.98	0.90	0.81–0.97
Ratios of all peptides	0.90	0.81–0.97	0.88	0.77–0.96

[a] Calculations of ICCs and 95% confidence intervals (CI) were performed separately for proteins from each retina using the PASW software as described in Experimental Procedures.

[b] Transducin, known to translocate away from rod outer segments upon illumination, was excluded from this dataset.
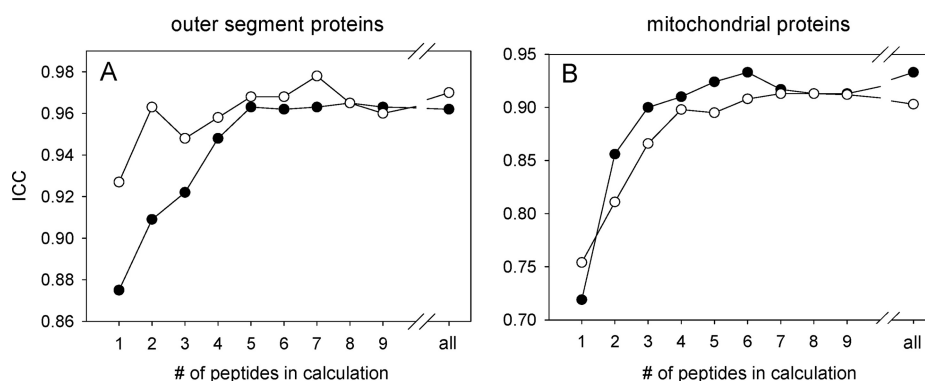

FIG. 3. **The dependence of protein quantification accuracy on the number of peptides used in the "sum of intensities" algorithm.** Protein distribution profiles for phototransduction and mitochondrial proteins were generated using the sum of intensities algorithm taking from one to nine most intense peptides into calculation. The calculations were performed separately for each retina (retina #1 - closed symbols, retina #2 - open symbols) for proteins shown in Fig. 2, except that transducin was omitted from the dataset in retina #2 because of its light-driven translocation from outer segments. The ICC values were calculated for each protein group using one through nine of the most intense peptides, as well as all peptides identified for each protein (see Experimental Procedures for computational details).

The first protein group included six phototransduction proteins localized exclusively to rod outer segments (Fig. 2; Table I), and indeed each protein quantification algorithm yielded distribution profiles peaking in the several most distal sections expected to represent rod outer segments. Interestingly, even algorithm #1 based on the single most intense peptide showed a fair degree of cross-correlation among individual proteins (ICC = 0.88; Fig. 2A). However, the ICC values were higher for each other algorithm we used, with the best cross-correlation obtained with algorithm #3 summing the intensities of all peptides from a given protein (Fig. 2E; ICC = 0.96), and the other two falling slightly behind (ICCs of 0.92 and 0.89 for algorithms #2 and #4, respectively; Fig. 2C, G). Repeating this analysis for sections obtained from the second retina yielded comparable results (Table I).

We next quantified a randomly chosen subset of eight mitochondrial proteins (Figs. 2B, D, F, H; Table I). Their distribution profiles in photoreceptors are rather complex: the majority resides in the inner segment and a minority in the synaptic terminal (see cartoon above Fig. 2B), reflected by lower absolute ICC values than for phototransduction pro-

teins. However, the relative ranking among the four protein quantification algorithms was essentially the same: the best cross-correlation was obtained by summing the intensities of all peptides, algorithms #2 and #4 provided intermediate results, and the worst cross-correlation was obtained using the single-peptide approach.

We also addressed how the reliability of the "sum of intensities" protein quantification algorithm depends on the number of peptides used in calculations. The quantities of phototransduction and mitochondrial proteins in each section were recalculated taking between one and nine most intense peptides into account, and the ICC values were determined as above (Fig. 3). All plots displayed an upward trend with ICC values improving significantly by including a second and third peptide and reaching saturation at ~5–6 peptides, which appears to be an optimal number for this analysis, at least for the type of tissue samples and instrumentation used in our study. These results are generally consistent with predictions by Carrillo *et al.* (52), whose bioinformatics analysis and experiments using a relatively simple protein mixture indicated that the "sum of intensities" algorithm (#3) produces more accurate
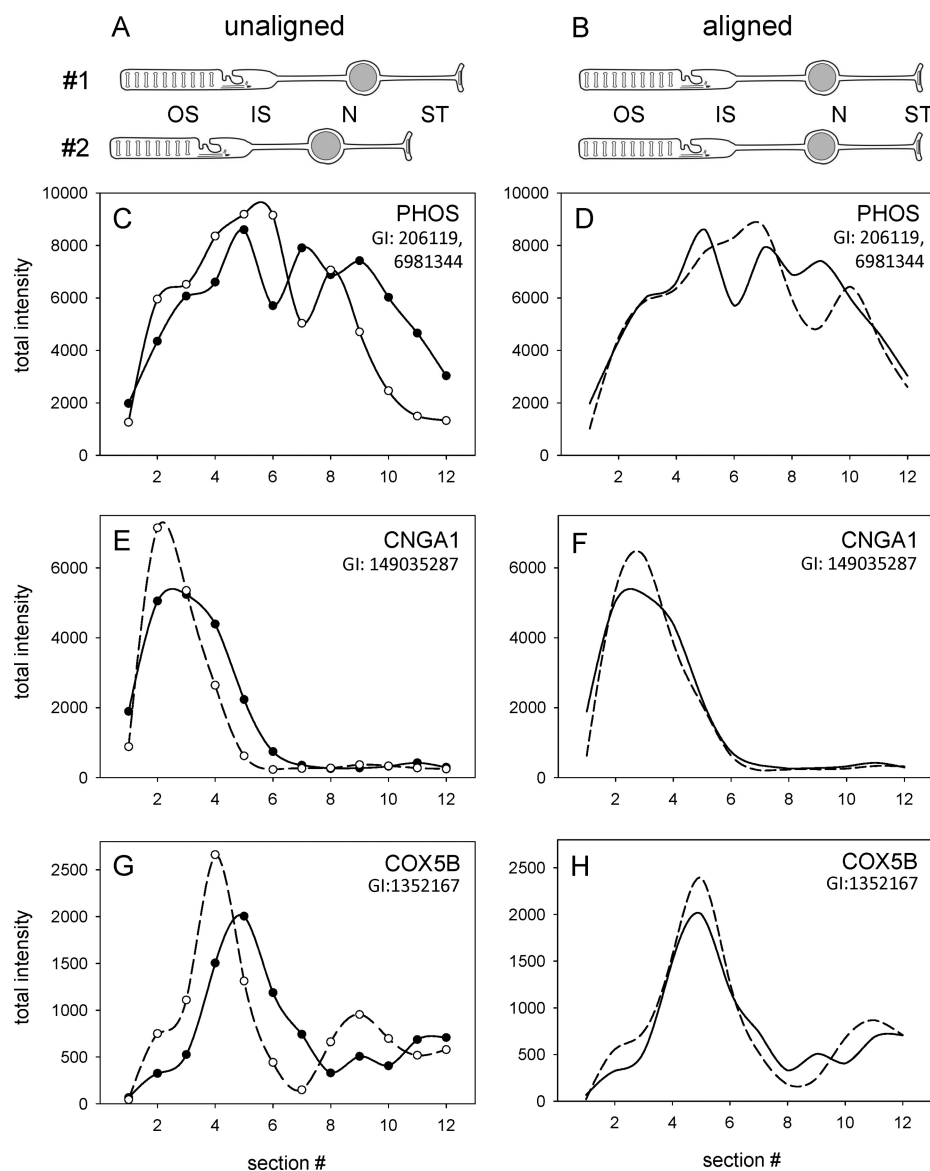
FIG. 4. **Data alignment among the protein distribution profiles obtained from two retinas.** *A* and *B*, Cartoons illustrating the presumed misalignment between the two tangentially sectioned retinas (*A*), compared with "perfect" alignment (*B*). *C*, Distribution profiles of phosducin in sections from each retina calculated by the sum of intensities algorithm. *D*, Phosducin distribution profile from retina #2 aligned to fit the profile from retina #1. *E* and *F*, original and aligned distribution profiles for the α-subunit of the cGMP-gated channel, CNG-α1 (the mean square error value was reduced from 1.37×10^7 to 6.22×10^6). *G* and *H*, Original and aligned distribution profiles for cytochrome C oxidase subunit V (the mean square error value was reduced from 4.75×10^4 to 7.43×10^3). Data for retina #1 are represented by a solid line; data for retina #2 are represented by a dashed line.

estimates of relative protein abundance than the "average of ratios" approach (#4). Our data extended this conclusion to an example of a more complex biological system. We should also stress that the idea to validate protein quantification algorithms by correlating profiles of proteins known to exist in fixed stoichiometric ratios in multiple samples is universally applicable to essentially any type of biological sample.

Averaging Protein Distribution Profiles between Two Retinas—We used the sum of intensities algorithm to generate distribution profiles for all identified proteins in each retina (supplemental Table 1, bold values). To preserve any potentially useful information, we did not set any thresholds on the minimal number of peptides or minimal peptide intensity, although we realize that the accuracy of protein profiles obtained on the basis of one or few peptides might require particularly careful verification in any follow-up studies.

To improve reliability of this analysis, we averaged the protein profiles between two retinas. This necessitated accounting for any differences in tissue alignment encountered upon freezing and sectioning of each retina. As described under "Experimental Procedures," two kinds of tissue distortion (tissue compression and unpredictability of the first section thickness; Fig. 4*A*), could be compensated mathematically. This was achieved by aligning the distribution profiles of phosducin, a marker protein chosen on the criteria of high abundance, exclusive expression in photoreceptors and distribution throughout the entire photoreceptor length (27, 43). Examination of each phosducin profile (Fig. 4*C*) suggested that the photoreceptor layer in retina #2 was more compressed than in retina #1 and slightly shifted to a lower section number. To account for both distortions, we modeled phosducin profiles as piecewise cubic polynomials
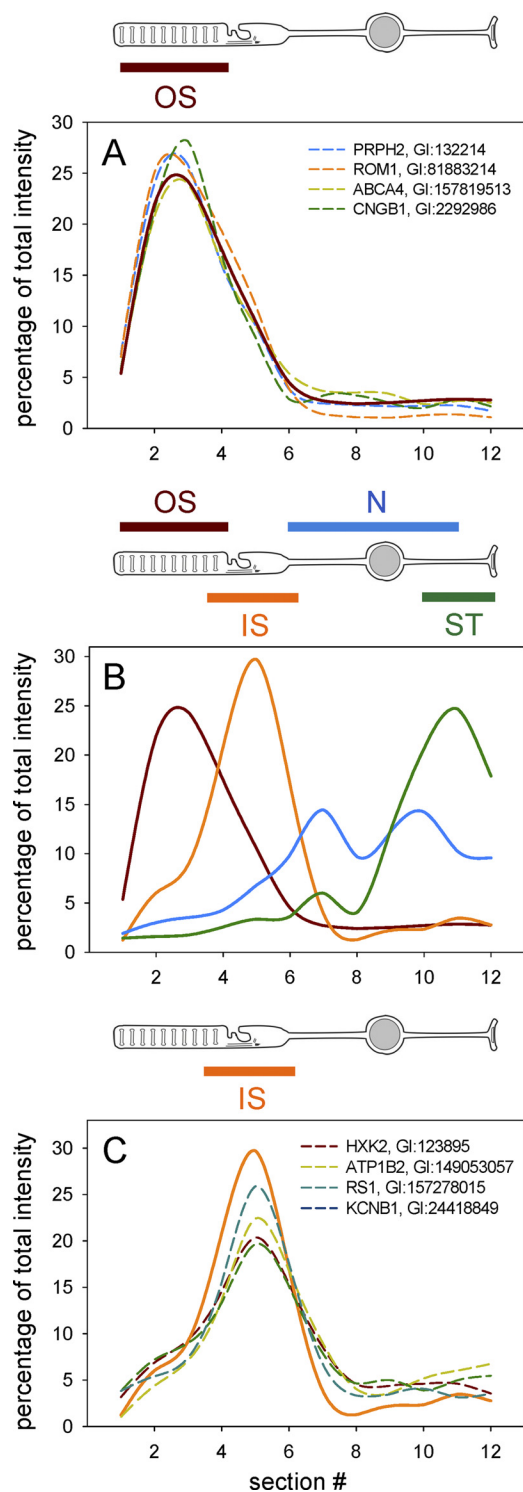
FIG. 5. **Distribution profiles of photoreceptor proteins representing different subcellular compartments.** Protein distribution profiles were calculated for each retina using the sum of intensities algorithm and averaged among the retinas after applying the alignment procedure shown in Fig. 4. *A*, The template profile for rod outer segment-specific proteins (*solid brown* line obtained by averaging the profiles of the α-subunit of cGMP phosphodiesterase, rhodopsin kinase, RGS9, the α-subunit of cyclic nucleotide gated channel and

and applied a scaled linear model to align the profiles, as described under "Experimental Procedures" (Fig. 4*D*), reducing the mean squared error between the retinas from 5×10^6 to 1.4×10^6. Applying the same correction parameters to other proteins yielded very closely matching profiles, as exemplified in Fig. 4*E*–4*H* for two abundant proteins (CNG-α1 and COX5B) residing in different parts of the photoreceptor cell. In all subsequent figures, we present averaged corrected protein profiles in the physical space of retina #1.

Distribution Profiles of Proteins Representing Different Subcellular Compartments of Photoreceptors—We defined the positions of major photoreceptor compartments in the proteome map using protein markers displaying highly restrictive localization patterns. In principle, this approach is similar to that of mapping organelles separated by centrifugation on a sucrose density gradient (53). For example, we generated a template profile for rod outer segments by averaging the individual profiles of five phototransduction proteins (Fig. 5*A*; *solid line*). Dashed lines in the same figure demonstrate that this template is a strong predictor of the distribution profiles for other proteins known to be confined to outer segments. We should note that a small group of signaling proteins, most importantly arrestin and transducin, change their distributions between the outer segments and the rest of the photoreceptor cell in a light-dependent manner, with arrestin moving into and transducin out of the outer segment (54). Although a detailed analysis of this phenomenon was not a focus of the present study, the distribution patterns of both arrestin and transducin were in good agreement with results obtained by other methods (supplemental Table 1), serving as an internal control that the expected protein distribution differences between the two retinas were clearly detected.

A similar approach was used to generate templates for proteins representing photoreceptor inner segments, the nuclear layer and the synaptic region (Fig. 5*B*). Although generating nuclear and synaptic templates was a straightforward task accomplished on the basis of randomly chosen abundant proteins representing each compartment, generating a template for the inner segment was challenging because most proteins residing there are also present in other parts of the

type E guanylate cyclase) and profiles of four other outer segment-specific proteins (*dashed lines*) listed and color-coded in the panel. *B*, Template profiles for outer segments (*brown*), inner segments (*orange*; based on rootletin), nuclear layer (*blue*; based on averaging profiles of heterogeneous nuclear ribonucleoprotein F, acidic nuclear phosphoprotein 32, nucleolin, IMP dehydrogenase, and small nuclear ribonucleoprotein D1), and synaptic termini (*green*; based on averaging profiles of synaptophysin, synaptic vesicle protein, Rab-3A, C-terminal binding protein 2 and vesicle-associated membrane protein 2). *C*, The template profile for rod inner segments (a solid orange line) and profiles of four other proteins closely matching this profile (*dashed lines*) listed and color-coded in the panel. For each panel, the subcellular localizations of individual protein groups are indicated by the bars next to the photoreceptor cell cartoons.
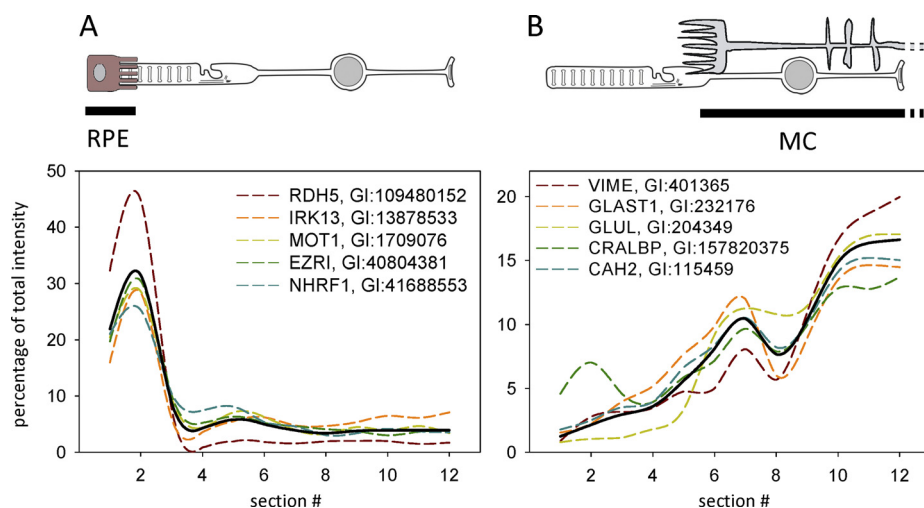
FIG. 6. **Distribution profiles of proteins representing the retinal pigment epithelium and Müller cells.** Profiles were calculated for each retina using the sum of intensities algorithm and averaged between the two retinas after applying the alignment procedure shown in Fig. 4. The template profiles for the retinal pigment epithelium (*A*) and Müller cells (*B*) are shown as black solid lines. Each profile was calculated by averaging the profiles of individual proteins listed in the panels and shown as dashed lines. Note that CRALBP was not used in template calculations because of its presence in both cell types. The localization of each cell relative to photoreceptors is shown in cartoons above each panel. Abbreviations: RPE, retinal pigment epithelium; MC, Müller cell.

cell. A rare exception is rootletin, a cytoskeletal protein thought to support the structural integrity of the inner-outer segment junction (55). The distribution profile of rootletin (Fig. 5*B*; *orange line*) was similar to the inner segment-specific peak of mitochondrial protein profiles, but unlike most mitochondrial proteins did not display a notable second peak at the synaptic terminal (*e.g.* Fig. 2*F*). To determine whether other proteins in our database have profiles similar to rootletin, we calculated the level of overlap between the rootletin template and averaged profiles of all other database entries. The proteins quantified on the basis of at least two peptides and displaying at least 80% overlap with rootletin are listed in supplemental Table 2. Although most represent mitochondrial proteins, because of their dominant peak in inner segments, several other hits were revealed, most notably the voltage-gated K^+ channel and retinoschisin (Fig. 5*C*). The former was shown to be expressed in photoreceptors (56) and the latter is known to be a part of the interphotoreceptor matrix (57). However the highly restricted localization patterns observed in Fig. 5*C* have not previously been established for either protein. On the other hand, the $\beta 2$ subunit of Na^+/K^+ ATPase was previously shown to be restricted to the inner segments (58), and this pattern was indeed confirmed in Fig. 5*C*. Another interesting example, hexokinase II, will be analyzed in detail below.

In addition to photoreceptors, the outer retina contains parts of two non-neuronal cell types, the Müller glial cells and the retinal pigment epithelium. The processes of the pigment epithelium extend into the space between rod and cone outer segments and, indeed, several proteins from the pigment epithelium were found in the first two sections of our map representing the outer segment tips (Fig. 6*A*). Müller cells span their cell bodies throughout the entire retina up to the border between photoreceptor inner segments and nuclei (called the outer limiting membrane); their thin microvilli penetrate even further into the space between inner segments. Accordingly, several Müller cell-specific proteins were present in our map, displaying distribution profiles reflecting this anatomical pattern (Fig. 6*B*). One protein, the cellular retinal aldehyde binding protein (CRALBP), is known to be expressed in both Müller cells and the pigment epithelium (59); in fact, the profile of CRALBP, but not other proteins from Müller cells contained an additional small peak in the outmost sections.

Cellular Distribution Patterns of Glycolytic Enzymes—Photoreceptors are among the most metabolically active cells in the body. In the dark, they need energy to power ion pumps maintaining both the circulating dark current and Ca^{2+} flux for synaptic transmission. In the light, they expend significant energy to support phototransduction (see (60, 61) for recent detailed analyses). It has been long known that glycolysis plays a critical role in fulfilling these energy needs (62). Glucose reaches the outer retina from the blood, passing the layer of pigment epithelium cells with the aid of facilitative glucose transporter Glut1 (63, 64). The same transporter is used for glucose entry into photoreceptor cells, where it is expressed in inner segments and synaptic terminals, but not outer segments, as demonstrated in our recent study (65). We now used the photoreceptor proteome map to investigate the intracellular sites of subsequent glucose metabolism by analyzing distribution patterns for the entire set of glycolytic enzymes (Fig. 7).

The Identity and Localization of Hexokinase Isoforms—Our immediate surprising finding was that, unlike the majority of

FIG. 7. **The distribution of glycolytic enzymes in the retina.** *A*, Distribution profiles of eleven glycolytic enzymes identified in the photoreceptor proteome map. The color coding of individual profiles is indicated to the right of the figure. The profiles of proteins further investigated by immunohistochemistry are shown as solid lines and the profiles of other proteins as dashed lines. *B*, Condensed schematic of the glycolytic pathway, highlighting the reactions catalyzed by hexokinase and triosephosphate isomerase. *C*, Cartoon of a photoreceptor cell aligned with proteome profiles in panel *A* and retina immunostainings in panels *D–G*. *D–G*, Immunostaining of retina cross-sections with antibodies against hexokinase I (*D*), hexokinase II (*E*), triosephosphate isomerase (*F*) and GAPDH (*G*). The individual panels are aligned by the position of the outer limiting membrane, indicated by an arrow below panel *G*. Abbreviations: OS, outer segments; IS, inner segments; ONL, outer nuclear layer; N, nucleus: ST, synaptic terminal; OPL, outer plexiform layer; INL, inner nuclear layer; IPL, inner plexiform layer; GC, ganglion cell layer.
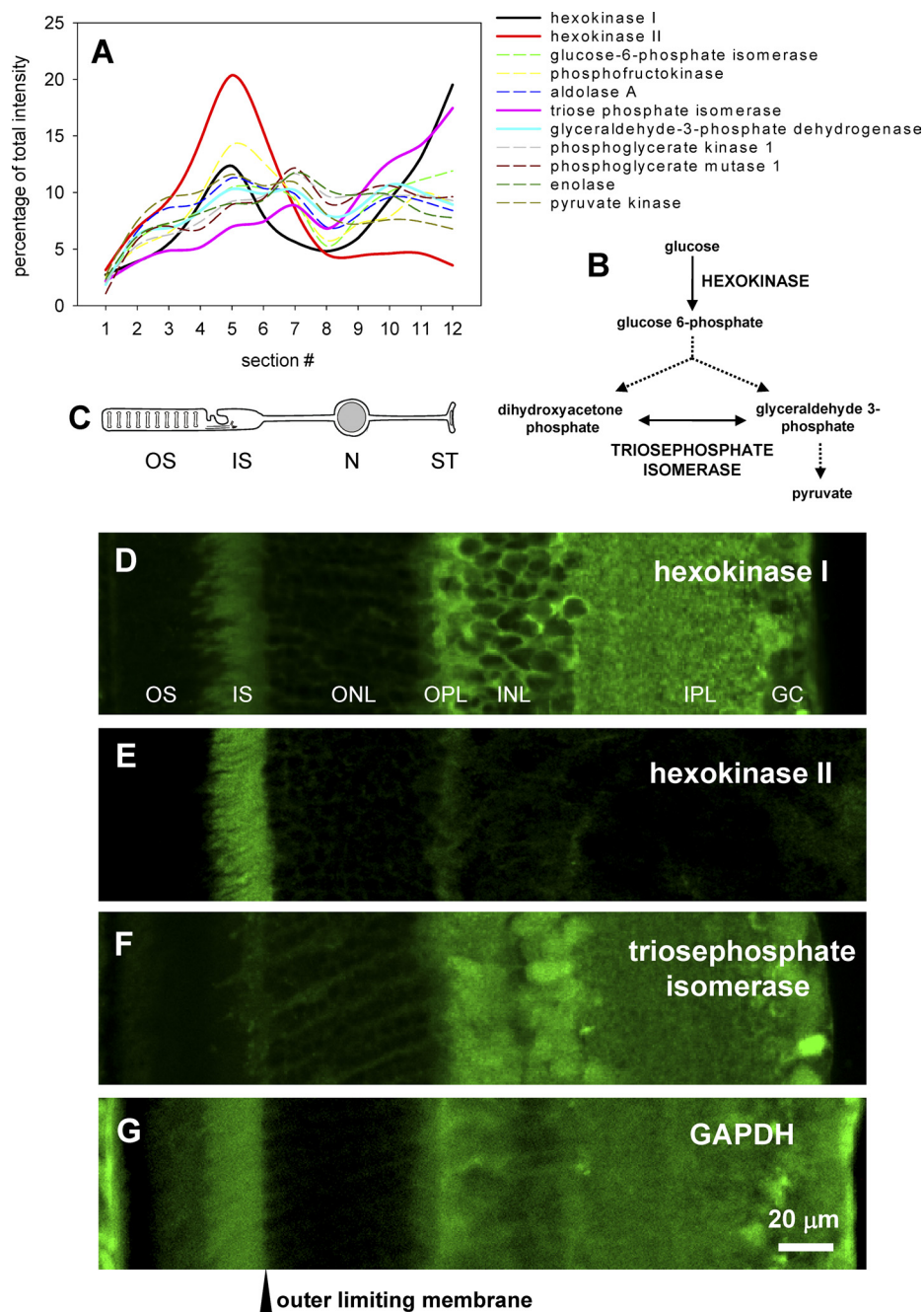
neurons, photoreceptors express hexokinase II in addition to the previously found hexokinase I (66). Furthermore, the distribution profiles of each hexokinase isoform were distinctly different from those for the majority of glycolytic enzymes (Fig. 7*A*). The latter displayed profiles suggesting an even distribution throughout the entire cytoplasmic volumes of photoreceptors and neighboring cells. They resembled the distribution of phosducin (Fig. 4), except for a higher abundance in sections 10–12 containing significant amounts of material from non-photoreceptor cells, consistent with these proteins being expressed in adjacent cell types as well. In contrast, the

profiles for each hexokinase had a large peak in the inner segment, likely reflecting their established pattern of mitochondrial association ((67; reviewed in (68, 69)). Hexokinase I displayed a second, even larger peak in sections 10–12, whereas hexokinase II was confined almost entirely to the inner segments, resembling the profile of rootletin (Fig. 5*C*).

To elaborate on these observations, we immunostained retina cross-sections with antibodies specifically recognizing each hexokinase isoform and found that each staining pattern closely matched its proteomic profile. Hexokinase I was expressed most abundantly outside the photoreceptor layer,

although it was also found in photoreceptor inner segments (Fig. 7D; see also (66)). In contrast, almost all hexokinase II was found in inner segments, with a very small additional signal in photoreceptor synapses and essentially no staining in other retinal cells (Fig. 7E). For comparison, we immunostained retina sections with an antibody against glyceraldehyde-3-phosphate dehydrogenase (GAPDH), the proteomic profile of which was representative of the majority of glycolytic enzymes (Fig. 7G). The staining pattern for GAPDH differed from both hexokinase isoforms and was indeed consistent with an even cytoplasmic distribution in photoreceptors and other retina cells.

The presence of hexokinase II and the mitochondria-associated localization pattern for both isoforms likely reflect the unique properties of glucose metabolism in photoreceptors. Hexokinases catalyze the first step in glycolysis—the phosphorylation of glucose to produce glucose-6-phosphate (Fig. 7B)—which is essential for intracellular glucose retention because phosphorylated glucose cannot undergo reversible transport through the plasma membrane. Hexokinase I is ubiquitously expressed in neuronal tissues, whereas hexokinase II is typically found in myocytes and cancer cells known to be particularly dependent on anaerobic energy metabolism (reviewed in (70, 71)). The latter is attributed to the higher catalytic activity of hexokinase II and its activation through mitochondrial association (70). Our finding that photoreceptors, but not other cells in the retina, express predominantly hexokinase II suggests that they also benefit from utilizing this more versatile isoform in order to keep up with the high level of energy metabolism.

We should also note that the lack of either hexokinase in the outer segment hints why outer segments are also deprived of the Glut1 glucose transporter (65). Glucose phosphorylation by hexokinase is required to trap glucose inside the cell because glucose-6-phosphate cannot escape the cell through the same transporter. Therefore, direct glucose entry into the outer segment compartment devoid of hexokinases would not result in its intracellular accumulation. Instead, glucose enters the cell in the inner segment, where it is converted into glucose-6-phosphate by hexokinases and can undergo further metabolism in both the inner and outer segments.

The Localization of Triosephosphate Isomerase—The third glycolytic enzyme with a profile distinctly different from the majority of this group was triosephosphate isomerase. Its proteomic profile displayed a steady upward trend from outer segments to synapses (Fig. 7A). Immunostaining revealed that the abundance of this enzyme in photoreceptors is very low compared with other cells. At a staining intensity providing bright signals in the inner retina, we observed essentially no staining in outer segments and little staining around the outer limiting membrane and around the nuclei, a pattern more consistent with staining of Müller cells than photoreceptors (Fig. 7F).

The role of triosephosphate isomerase in glycolysis is to convert dihydroxyacetone phosphate into glyceraldehyde-3-phosphate, after both are produced upon the cleavage of fructose-1,6-bisphosphate by fructose bisphosphate aldolase (Fig. 7B). Therefore, low abundance of triosephosphate isomerase in photoreceptors is predicted to result in an elevated level of dihydroxyacetone phosphate compared with other retina cells. Although we can only speculate about the functional significance of such a phenomenon, one possibility is that it relates to phospholipid biosynthesis, as dihydroxyacetone phosphate serves as a precursor of glycerol-3-phosphate, the phospholipid backbone (72). Photoreceptors synthesize phospholipids at an unusually high rate because of the constant renewal of their outer segment membranes (73, 74). The surface area of these membranes produced daily in a rat retina exceeds the surface area of the eyeball by over 50-fold (75). This makes it plausible that an elevated dihydroxyacetone phosphate concentration would facilitate this biosynthetic pathway.

As a final note in regards to glycolytic enzymes in the outer retina, we should mention that our data reject a recent claim that photoreceptors, retinal pigment epithelium and Müller cells lack glucose-6-phosphate isomerase-1 (76). We identified 36 peptides from this protein, showed that its distribution profile matches the majority of glycolytic enzymes and found no evidence that any other glucose-6-phosphate isomerase isoform is present in the outer retina within the detectability limits of our assay.

Concluding Remarks—The data presented in this study illustrate the power of combining label-free quantitative proteomics with subcellular fragmentation of a layered tissue by serial sectioning. Based on this approach, we generated a proteome map describing the distribution profiles of hundreds of proteins representing the photoreceptor layer of the retina. We used this map to examine the subcellular composition of glycolytic enzymes and revealed previously unknown patterns of isoform composition and distribution, all suggesting unique mechanistic features employed by photoreceptor cells to meet their high energetic and metabolic needs. This is unlikely to be the sole discovery embedded within our protein map, which is presented in a format that can be mined by other investigators studying other aspects of photoreceptor function.

Our approach to studying the photoreceptor proteome differs from that used in several recent reports. Most previous studies focused on analyzing the protein composition of rod outer segments, the organelle readily separable from the rest of the retina by centrifugation procedures (77–79). Others attempted to obtain proteomes of the whole photoreceptor cell by mechanical separation of the retina layers (80), obtaining tangential sections containing the entire photoreceptor layer (81), or by analyzing the difference between proteomes of the normal retinas and those in which rods underwent inherited degeneration (82). Unlike any of these strategies,

thin serial sectioning allowed us to conduct protein identification and quantification in all the individual subcellular compartments of these cells, each defined by profile shapes of marker proteins. Our approach is also different from any "snapshot" proteomes of fractionated organelles, which rarely contain any intrinsic hints to distinguish between the proteins actually residing in an organelle of interest and those introduced from contaminations. For example, each published rod outer segment proteome contained multiple entries of mitochondrial and nuclear proteins, despite their actual absence from outer segments (77–79). Sections representing the outer segments in our study were not free of contamination either, but unlike in snapshot proteomes, the distinction between outer segment-specific proteins and contaminants from other cellular compartments could be made on the basis of each protein's overall distribution profile.

Finally, we would like to stress that the approach developed in this study can serve as a guide for generating similar proteome databases addressing protein distribution profiles in essentially any layered tissue. Our work represents a case study exploring both general methodology of protein quantification and simple computational corrections for the unavoidable problem of tissue distortion during cryosectioning. In fact, the retina is among the smallest layered tissues in our body; applying the same approach to larger tissues is likely to yield deeper protein coverage, while being less technically challenging. Furthermore, a similar strategy could be very useful in the proteomic investigation of specimens where quantification of proteins with high spatial resolution at a margin is important, for example the margins of invasive tumors.

¶ To whom correspondence should be addressed: Vadim Y. Arshavsky, Duke University Eye Center, AERI, 2351 Erwin Road, Box 3802 Durham, NC 27710. Tel.: (919) 668-5391; Fax: (919) 684-3826; E-mail: vadim.arshavsky@duke, or Nikolai P. Skiba, Duke University Eye Center, AERI, 2351 Erwin Road, Box 3802 Durham, NC 27710. Tel.: (919) 668-5621; Fax: (919) 684-3826; E-mail: nikolai.skiba@duke.edu.

REFERENCES

1. Rodiek, R. W. (1973) *The Vertebrate Retina. Principles of Structure and Function*, Freeman, San Francisco
2. Umar, A., Luider, T. M., Foekens, J. A., and Pasa-Tolic, L. (2007) NanoLC-FT-ICR MS improves proteome coverage attainable for approximately 3000 laser-microdissected breast carcinoma cells. *Proteomics* **7,** 323–329
3. Moulédous, L., Hunt, S., Harcourt, R., Harry, J., Williams, K. L., and Gutstein, H. B. (2003) Navigated laser capture microdissection as an alternative to direct histological staining for proteomic analysis of brain samples. *Proteomics* **3,** 610–615
4. Ornstein, D. K., Gillespie, J. W., Paweletz, C. P., Duray, P. H., Herring, J., Vocke, C. D., Topalian, S. L., Bostwick, D. G., Linehan, W. M., Petricoin, E. F., 3rd, and Emmert-Buck, M. R. (2000) Proteomic analysis of laser capture microdissected human prostate cancer and in vitro prostate cell lines. *Electrophoresis* **21,** 2235–2242
5. Zang, L., Palmer Toy, D., Hancock, W. S., Sgroi, D. C., and Karger, B. L. (2004) Proteomic analysis of ductal carcinoma of the breast using laser capture microdissection, LC-MS, and 16O/18O isotopic labeling. *J. Proteome Res.* **3,** 604–612
6. Wulfkuhle, J. D., Paweletz, C. P., Steeg, P. S., Petricoin, E. F., 3rd, and Liotta, L. (2003) Proteomic approaches to the diagnosis, treatment, and monitoring of cancer. *Adv. Exp. Med. Biol.* **532,** 59–68
7. Wulfkuhle, J. D., McLean, K. C., Paweletz, C. P., Sgroi, D. C., Trock, B. J., Steeg, P. S., and Petricoin, E. F., 3rd (2001) New approaches to proteomic analysis of breast cancer. *Proteomics* **1,** 1205–1215
8. Maddalo, G., Petrucci, F., Iezzi, M., Pannellini, T., Del Boccio, P., Ciavardelli, D., Biroccio, A., Forli, F., Di Ilio, C., Ballone, E., Urbani, A., and Federici, G. (2005) Analytical assessment of MALDI-TOF Imaging Mass Spectrometry on thin histological samples. An insight in proteome investigation. *Clin. Chim. Acta* **357,** 210–218
9. Meistermann, H., Norris, J. L., Aerni, H. R., Cornett, D. S., Friedlein, A., Erskine, A. R., Augustin, A., De Vera Mudry, M. C., Ruepp, S., Suter, L., Langen, H., Caprioli, R. M., and Ducret, A. (2006) Biomarker discovery by imaging mass spectrometry: transthyretin is a biomarker for gentamicin-induced nephrotoxicity in rat. *Mol. Cell. Proteomics* **5,** 1876–1886
10. Lemaire, R., Menguellet, S. A., Stauber, J., Marchaudon, V., Lucot, J.-P., Collinet, P., Farine, M.-O., Vinatier, D., Day, R., Ducoroy, P., Salzet, M., and Fournier, I. (2007) Specific MALDI imaging and profiling for biomarker hunting and validation: fragment of the 11S proteasome activator complex, Reg alpha fragment, is a new potential ovary cancer biomarker. *J. Proteome Res.* **6,** 4127–4134
11. Lemaire, R., Desmons, A., Tabet, J. C., Day, R., Salzet, M., and Fournier, I. (2007) Direct analysis and MALDI imaging of formalin-fixed, paraffin-embedded tissue sections. *J. Proteome Res.* **6,** 1295–1305
12. Wisztorski, M., Lemaire, R., Stauber, J., Menguelet, S. A., Croix, D., Mathé, O. J., Day, R., Salzet, M., and Fournier, I. (2007) New developments in MALDI imaging for pathology proteomic studies. *Curr. Pharm. Des.* **13,** 3317–3324
13. Fournier, I., Wisztorski, M., and Salzet, M. (2008) Tissue imaging using MALDI-MS: a new frontier of histopathology proteomics. *Expert Review of Proteomics* **5,** 413–424
14. Strittmatter, E. F., Ferguson, P. L., Tang, K., and Smith, R. D. (2003) Proteome analyses using accurate mass and elution time peptide tags with capillary LC time-of-flight mass spectrometry. *J. Am. Soc. Mass. Spectrom.* **14,** 980–991
15. Pasa-Tolić, L., Masselon, C., Barry, R. C., Shen, Y., and Smith, R. D. (2004) Proteomic analyses using an accurate mass and time tag strategy. *BioTechniques* **37,** 621–624,626–633, 636 passim
16. Silva, J. C., Denny, R., Dorschel, C. A., Gorenstein, M., Kass, I. J., Li, G. Z., McKenna, T., Nold, M. J., Richardson, K., Young, P., and Geromanos, S. (2005) Quantitative proteomic analysis by accurate mass retention time pairs. *Anal. Chem.* **77,** 2187–2200
17. Adkins, J. N., Monroe, M. E., Auberry, K. J., Shen, Y., Jacobs, J. M., Camp, D. G., 2nd, Vitzthum, F., Rodland, K. D., Zangar, R. C., Smith, R. D., and Pounds, J. G. (2005) A proteomic study of the HUPO Plasma Proteome Project's pilot samples using an accurate mass and time tag strategy. *Proteomics* **5,** 3454–3466
18. Zimmer, J. S., Monroe, M. E., Qian, W. J., and Smith, R. D. (2006) Advances in proteomics data analysis and display using an accurate mass and time tag approach. *Mass Spectrom. Rev.* **25,** 450–482
19. Tolmachev, A. V., Monroe, M. E., Purvine, S. O., Moore, R. J., Jaitly, N., Adkins, J. N., Anderson, G. A., and Smith, R. D. (2008) Characterization of strategies for obtaining confident identifications in bottom-up proteomics measurements using hybrid FTMS instruments. *Anal. Chem.* **80,** 8514–8525
20. Webb-Robertson, B. J. M., Cannon, W. R., Oehmen, C. S., Shah, A. R., Gurumoorthi, V., Lipton, M. S., and Waters, K. M. (2010) A support vector machine model for the prediction of proteotypic peptides for accurate mass and time proteomics. *Bioinformatics* **26,** 1677–1683
21. Kiebel, G. R., Auberry, K. J., Jaitly, N., Clark, D. A., Monroe, M. E., Peterson, E. S., Tolić, N., Anderson, G. A., and Smith, R. D. (2006) PRISM: a data

management system for high-throughput proteomics. *Proteomics* **6,** 1783–1790

22. Jaffe, J. D., Mani, D. R., Leptos, K. C., Church, G. M., Gillette, M. A., and Carr, S. A. (2006) PEPPeR, a platform for experimental proteomic pattern recognition. *Mol. Cell. Proteomics* **5,** 1927–1941

23. Cox, J., and Mann, M. (2008) MaxQuant enables high peptide identification rates, individualized p.p.b.-range mass accuracies and proteome-wide protein quantification. *Nat. Biotechnol.* **26,** 1367–1372

24. Neubert, H., Bonnert, T. P., Rumpel, K., Hunt, B. T., Henle, E. S., and James, I. T. (2008) Label-free detection of differential protein expression by LC/MALDI mass spectrometry. *J. Proteome Res.* **7,** 2270–2279

25. Szél, A., and Röhlich, P. (1992) Two cone types of rat retina detected by anti-visual pigment antibodies. *Exp. Eye Res.* **55,** 47–52

26. Sokolov, M., Lyubarsky, A. L., Strissel, K. J., Savchenko, A. B., Govardovskii, V. I., Pugh, E. N., Jr., and Arshavsky, V. Y. (2002) Massive light-driven translocation of transducin between the two major compartments of rod cells: a novel mechanism of light adaptation. *Neuron* **34,** 95–106

27. Sokolov, M., Strissel, K. J., Leskov, I. B., Michaud, N. A., Govardovskii, V. I., and Arshavsky, V. Y. (2004) Phosducin facilitates light-driven transducin translocation in rod photoreceptors. Evidence from the phosducin knockout mouse. *J. Biol. Chem.* **279,** 19149–19156

28. Hong, D. H., Pawlyk, B., Sokolov, M., Strissel, K. J., Yang, J., Tulloch, B., Wright, A. F., Arshavsky, V. Y., and Li, T. (2003) RPGR isoforms in photoreceptor connecting cilia and the transitional zone of motile cilia. *Invest. Ophthalmol Vis Sci.* **44,** 2413–2421

29. Lobanova, E. S., Finkelstein, S., Song, H., Tsang, S. H., Chen, C. K., Sokolov, M., Skiba, N. P., and Arshavsky, V. Y. (2007) Transducin translocation in rods is triggered by saturation of the GTPase-activating complex. *J. Neurosci.* **27,** 1151–1160

30. Strissel, K. J., Sokolov, M., Trieu, L. H., and Arshavsky, V. Y. (2006) Arrestin translocation is induced at a critical threshold of visual signaling and is superstoichiometric to bleached rhodopsin. *J. Neurosci.* **26,** 1146–1153

31. Paweletz, C. P., Wiener, M. C., Bondarenko, A. Y., Yates, N. A., Song, Q., Liaw, A., Lee, A. Y., Hunt, B. T., Henle, E. S., Meng, F., Sleph, H. F., Holahan, M., Sankaranarayanan, S., Simon, A. J., Settlage, R. E., Sachs, J. R., Shearman, M., Sachs, A. B., Cook, J. J., and Hendrickson, R. C. (2010) Application of an end-to-end biomarker discovery platform to identify target engagement markers in cerebrospinal fluid by high resolution differential mass spectrometry. *J. Proteome Res.* **9,** 1392–1401

32. Sietsema, K. E., Meng, F., Yates, N. A., Hendrickson, R. C., Liaw, A., Song, Q., Brass, E. P., and Ulrich, R. G. (2010) Potential biomarkers of muscle injury after eccentric exercise. *Biomarkers* **15,** 249–258

33. Lomenick, B., Hao, R., Jonai, N., Chin, R. M., Aghajan, M., Warburton, S., Wang, J., Wu, R. P., Gomez, F., Loo, J. A., Wohlschlegel, J. A., Vondriska, T. M., Pelletier, J., Herschman, H. R., Clardy, J., Clarke, C. F., and Huang, J. (2009) Target identification using drug affinity responsive target stability (DARTS). *Proc. Natl. Acad. Sci. U.S.A.* **106,** 21984–21989

34. Chan, E. Y., Sutton, J. N., Jacobs, J. M., Bondarenko, A., Smith, R. D., and Katze, M. G. (2009) Dynamic host energetics and cytoskeletal proteomes in human immunodeficiency virus type 1-infected human primary CD4 cells: analysis by multiplexed label-free mass spectrometry. *J. Virol.* **83,** 9283–9295

35. Lee, A. Y., Paweletz, C. P., Pollock, R. M., Settlage, R. E., Cruz, J. C., Secrist, J. P., Miller, T. A., Stanton, M. G., Kral, A. M., Ozerova, N. D., Meng, F., Yates, N. A., Richon, V., and Hendrickson, R. C. (2008) Quantitative analysis of histone deacetylase-1 selective histone modifications by differential mass spectrometry. *J. Proteome Res.* **7,** 5177–5186

36. Meng, F., Wiener, M. C., Sachs, J. R., Burns, C., Verma, P., Paweletz, C. P., Mazur, M. T., Deyanova, E. G., Yates, N. A., and Hendrickson, R. C. (2007) Quantitative analysis of complex peptide mixtures using FTMS and differential mass spectrometry. *J. Am. Soc. Mass. Spectrom.* **18,** 226–233

37. Nittis, T., Guittat, L., LeDuc, R. D., Dao, B., Duxin, J. P., Rohrs, H., Townsend, R. R., and Stewart, S. A. (2010) Revealing novel telomere proteins using in vivo cross-linking, tandem affinity purification, and label-free quantitative LC-FTICR-MS. *Mol. Cell. Proteomics* **9,** 1144–1156

38. Geromanos, S. J., Vissers, J. P., Silva, J. C., Dorschel, C. A., Li, G. Z., Gorenstein, M. V., Bateman, R. H., and Langridge, J. I. (2009) The detection, correlation, and comparison of peptide precursor and product ions from data independent LC-MS with data dependant LC-MS/MS. *Proteomics* **9,** 1683–1695

39. Li, G. Z., Vissers, J. P., Silva, J. C., Golick, D., Gorenstein, M. V., and Geromanos, S. J. (2009) Database searching and accounting of multiplexed precursor and product ion spectra from the data independent analysis of simple and complex peptide mixtures. *Proteomics* **9,** 1696–1719

40. Keller, A., Nesvizhskii, A. I., Kolker, E., and Aebersold, R. (2002) Empirical statistical model to estimate the accuracy of peptide identifications made by MS/MS and database search. *Anal. Chem.* **74,** 5383–5392

41. Nesvizhskii, A. I., Keller, A., Kolker, E., and Aebersold, R. (2003) A statistical model for identifying proteins by tandem mass spectrometry. *Anal. Chem.* **75,** 4646–4658

42. Shrout, P. E., and Fleiss, J. L. (1979) Intraclass correlations: uses in assessing rater reliability. *Psychol. Bull.* **86,** 420–428

43. Thulin, C. D., Howes, K., Driscoll, C. D., Savage, J. R., Rand, T. A., Baehr, W., and Willardson, B. M. (1999) The immunolocalization and divergent roles of phosducin and phosducin-like protein in the retina. *Mol. Vis.* **5,** 40

44. Bamberger, R. H., Eddins, S. L., and Nuri, V. (1994) Generalized symmetric extension for size-limited multirate filter banks. *IEEE Trans Image Process* **3,** 82–87

45. Herrmann, R., Lobanova, E. S., Hammond, T., Kessler, C., Burns, M. E., Frishman, L. J., and Arshavsky, V. Y. (2010) Phosducin Regulates Transmission at thePhotoreceptor-to-ON-Bipolar Cell Synapse. *J. Neurosci.* **30,** 3239–3253

46. Le Bihan, T., Goh, T., Stewart, II, Salter, A. M., Bukhman, Y. V., Dharsee, M., Ewing, R., and Wiśniewski, J. R. (2006) Differential analysis of membrane proteins in mouse fore- and hindbrain using a label-free approach. *J. Proteome Res.* **5,** 2701–2710

47. Silva, J. C., Denny, R., Dorschel, C., Gorenstein, M. V., Li, G. Z., Richardson, K., Wall, D., and Geromanos, S. J. (2006) Simultaneous qualitative and quantitative analysis of the Escherichia coli proteome: a sweet tale. *Mol. Cell. Proteomics* **5,** 589–607

48. Wang, G., Wu, W. W., Zeng, W., Chou, C. L., and Shen, R. F. (2006) Label-free protein quantification using LC-coupled ion trap or FT mass spectrometry: Reproducibility, linearity, and application with complex proteomes. *J. Proteome Res.* **5,** 1214–1223

49. Silva, J. C., Gorenstein, M. V., Li, G. Z., Vissers, J. P., and Geromanos, S. J. (2006) Absolute quantification of proteins by LCMSE: a virtue of parallel MS acquisition. *Mol. Cell. Proteomics* **5,** 144–156

50. Ono, M., Shitashige, M., Honda, K., Isobe, T., Kuwabara, H., Matsuzuki, H., Hirohashi, S., and Yamada, T. (2006) Label-free quantitative proteomics using large peptide data sets generated by nanoflow liquid chromatography and mass spectrometry. *Mol. Cell. Proteomics* **5,** 1338–1347

51. Saito, A., Nagasaki, M., Oyama, M., Kozuka-Hata, H., Semba, K., Sugano, S., Yamamoto, T., and Miyano, S. (2007) AYUMS: an algorithm for completely automatic quantitation based on LC-MS/MS proteome data and its application to the analysis of signal transduction. *BMC Bioinformatics* **8,** 15

52. Carrillo, B., Yanofsky, C., Laboissiere, S., Nadon, R., and Kearney, R. E. (2010) Methods for combining peptide intensities to estimate relative protein abundance. *Bioinformatics* **26,** 98–103

53. Foster, L. J., de Hoog, C. L., Zhang, Y., Zhang, Y., Xie, X., Mootha, V. K., and Mann, M. (2006) A mammalian organelle map by protein correlation profiling. *Cell* **125,** 187–199

54. Calvert, P. D., Strissel, K. J., Schiesser, W. E., Pugh, E. N., Jr., and Arshavsky, V. Y. (2006) Light-driven translocation of signaling proteins in vertebrate photoreceptors. *Trends Cell Biol.* **16,** 560–568

55. Yang, J., Liu, X., Yue, G., Adamian, M., Bulgakov, O., and Li, T. (2002) Rootletin, a novel coiled-coil protein, is a structural component of the ciliary rootlet. *J. Cell Biol.* **159,** 431–440

56. Yazulla, S., and Studholme, K. M. (1998) Differential distribution of Shaker-like and Shab-like K+-channel subunits in goldfish retina and retinal bipolar cells. *J. Comp. Neurol.* **396,** 131–140

57. Vijayasarathy, C., Takada, Y., Zeng, Y., Bush, R. A., and Sieving, P. A. (2007) Retinoschisin is a peripheral membrane protein with affinity for anionic phospholipids and affected by divalent cations. *Invest. Ophthalmol. Vis. Sci.* **48,** 991–1000

58. Schneider, B. G., Shyjan, A. W., and Levenson, R. (1991) Co-localization and polarized distribution of Na,K-ATPase alpha 3 and beta 2 subunits in photoreceptor cells. *J. Histochem. Cytochem.* **39,** 507–517

59. Bunt-Milam, A. H., and Saari, J. C. (1983) Immunocytochemical localization of two retinoid-binding proteins in vertebrate retina. *J. Cell Biol.* **97,** 703–712

60. Okawa, H., Sampath, A. P., Laughlin, S. B., and Fain, G. L. (2008) ATP consumption by mammalian rod photoreceptors in darkness and in light. *Curr. Biol.* **18,** 1917–1921

61. Linton, J. D., Holzhausen, L. C., Babai, N., Song, H., Miyagishima, K. J., Stearns, G. W., Lindsay, K., Wei, J., Chertov, A. O., Peters, T. A., Caffe, R., Pluk, H., Seeliger, M. W., Tanimoto, N., Fong, K., Bolton, L., Kuok, D. L., Sweet, I. R., Bartoletti, T. M., Radu, R. A., Travis, G. H., Zagotta, W. N., Townes-Anderson, E., Parker, E., Van der Zee, C. E., Sampath, A. P., Sokolov, M., Thoreson, W. B., and Hurley, J. B. (2010) Flow of energy in the outer retina in darkness and in light. *Proc. Natl. Acad. Sci. U.S.A.* **107,** 8599–8604

62. Hsu, S. C., and Molday, R. S. (1994) Glucose metabolism in photoreceptor outer segments. Its role in phototransduction and in NADPH-requiring reactions. *J. Biol. Chem.* **269,** 17954–17959

63. Takata, K., Kasahara, T., Kasahara, M., Ezaki, O., and Hirano, H. (1990) Erythrocyte/HepG2-type glucose transporter is concentrated in cells of blood-tissue barriers. *Biochem. Biophys. Res. Commun.* **173,** 67–73

64. Takata, K., Kasahara, T., Kasahara, M., Ezaki, O., and Hirano, H. (1992) Ultracytochemical localization of the erythrocyte/HepG2-type glucose transporter (GLUT1) in cells of the blood-retinal barrier in the rat. *Invest. Ophthalmol. Vis. Sci.* **33,** 377–383

65. Gospe, S. M., 3rd, Baker, S. A., and Arshavsky, V. Y. (2010) Facilitative glucose transporter Glut1 is actively excluded from rod outer segments. *J. Cell Sci.* **123**

66. Aslanukov, A., Bhowmick, R., Guruju, M., Oswald, J., Raz, D., Bush, R. A., Sieving, P. A., Lu, X., Bock, C. B., and Ferreira, P. A. (2006) RanBP2 modulates Cox11 and hexokinase I activities and haploinsufficiency of RanBP2 causes deficits in glucose metabolism. *PLoS Genet.* **2,** e177

67. Simurda, M., and Wilson, J. E. (1980) Localization of hexokinase in neural tissue: immunofluorescence studies on the developing cerebellum and retina of the rat. *J. Neurochem.* **35,** 58–66

68. Golshani-Hebroni, S. G., and Bessman, S. P. (1997) Hexokinase binding to mitochondria: a basis for proliferative energy metabolism. *J. Bioenerg. Biomembr.* **29,** 331–338

69. Mathupala, S. P., Ko, Y. H., and Pedersen, P. L. (2009) Hexokinase-2 bound to mitochondria: cancer's stygian link to the "Warburg Effect" and a pivotal target for effective therapy. *Semin. Cancer Biol.* **19,** 17–24

70. Wilson, J. E. (1995) *Hexokinases. Rev. Physiol. Biochem. Pharmacol.* **126,** 65–198

71. Cárdenas, M. L., Cornish-Bowden, A., and Ureta, T. (1998) Evolution and regulatory role of the hexokinases. *Biochim. Biophys. Acta* **1401,** 242–264

72. Agranoff, B. W., and Hajra, A. K. (1971) The acyl dihydroxyacetone phosphate pathway for glycerolipid biosynthesis in mouse liver and Ehrlich ascites tumor cells. *Proc. Natl. Acad. Sci. U.S.A.* **68,** 411–415

73. Insinna, C., and Besharse, J. C. (2008) Intraflagellar transport and the sensory outer segment of vertebrate photoreceptors. *Dev. Dyn.* **237,** 1982–1992

74. Sung, C. H., and Chuang, J. Z. The cell biology of vision. *J. Cell Biol.* **190,** 953–963

75. Mayhew, T. M., and Astle, D. (1997) Photoreceptor number and outer segment disk membrane surface area in the retina of the rat: stereological data for whole organ and average photoreceptor cell. *J. Neurocytol.* **26,** 53–61

76. Archer, S. N., Ahuja, P., Caffé, R., Mikol, C., Foster, R. G., van Veen, T., and von Schantz, M. (2004) Absence of phosphoglucose isomerase-1 in retinal photoreceptor, pigment epithelium and Muller cells. *Eur. J. Neurosci.* **19,** 2923–2930

77. Liu, Q., Tan, G., Levenkova, N., Li, T., Pugh, E. N., Jr., Rux, J. J., Speicher, D. W., and Pierce, E. A. (2007) The proteome of the mouse photoreceptor sensory cilium complex. *Mol. Cell. Proteomics* **6,** 1299–1317

78. Kwok, M. C., Holopainen, J. M., Molday, L. L., Foster, L. J., and Molday, R. S. (2008) Proteomics of photoreceptor outer segments identifies a subset of SNARE and Rab proteins implicated in membrane vesicle trafficking and fusion. *Mol. Cell. Proteomics* **7,** 1053–1066

79. Panfoli, I., Musante, L., Bachi, A., Ravera, S., Calzia, D., Cattaneo, A., Bruschi, M., Bianchini, P., Diaspro, A., Morelli, A., Pepe, I. M., Tacchetti, C., and Candiano, G. (2008) Proteomic analysis of the retinal rod outer segment disks. *J. Proteome Res.* **7,** 2654–2669

80. Nishizawa, Y., Komori, N., Usukura, J., Jackson, K. W., Tobin, S. L., and Matsumoto, H. (1999) Initiating ocular proteomics for cataloging bovine retinal proteins: microanalytical techniques permit the identification of proteins derived from a novel photoreceptor preparation. *Exp. Eye Res.* **69,** 195–212

81. McKay, G. J., Campbell, L., Oliver, M., Brockbank, S., Simpson, D. A., and Curry, W. J. (2004) Preparation of planar retinal specimens: verification by histology, mRNA profiling, and proteome analysis. *Mol. Vis.* **10,** 240–247

82. Cavusoglu, N., Thierse, D., Mohand-Saïd, S., Chalmel, F., Poch, O., Van-Dorsselaer, A., Sahel, J. A., and Léveillard, T. (2003) Differential proteomic analysis of the mouse retina: the induction of crystallin proteins by retinal degeneration in the rd1 mouse. *Mol. Cell. Proteomics* **2,** 494–505